buildings

MDPI

Article

Multi-Source Monitoring and Numerical Simulation Deformation on Highway Steep Slopes Under Rainfall Effects

Peijun Li [1], Qing Li [1], Qingshan Feng [1], Zhendong Huang [1], Xun Gan [2,*], Haibin Ding [2] and Changjie Xu [2]

[1] Guangdong Jiaoke Testing Co., Ltd., Guangzhou 510080, China
[2] Jiangxi Key Laboratory of Infrastructure Safety and Control in Geotechnical Engineering, East China Jiaotong University, Nanchang 330013, China
* Correspondence: 2022018085901087@ecjtu.edu.cn

Abstract: Rainfall is one of the most important factors affecting slope stability. This study employed multi-source monitoring devices to observe the slope displacements in real time under rainfall infiltration and performed numerical simulations to investigate the effects of different rainfall conditions and anti-slip pile configurations on slope stability. Specifically, multi-source monitoring operations were conducted on the high and steep slopes along the Yunmao Expressway. Real-time data on slope deformation, rainfall, and displacement at the tops of anti-slip piles were collected and analyzed, and numerical simulations were conducted using Geo Studio finite-element software. The findings indicated that abrupt deformation of slopes occurs once a threshold rainfall amount is surpassed and sustained over a specific duration. Slope displacement decreased with increasing slope depth above the potential slip fracture surface, with a more rapid reduction in deformation rates observed in slopes reinforced with anti-slip piles. For equivalent rainfall amounts, short-duration, intense rainfalls led to a rapid decrease in the slope safety factor, which also recovered rapidly once the rainfall ceased, in contrast to long-duration, mild rainfalls. The presence and location of anti-slip piles significantly influenced slope stability; therefore, project implementation should carefully consider factors such as cost and duration for optimal decision making.

Keywords: high and steep slope; multi-source monitoring; slope displacement and deformation; rainfall infiltration; safety factor

check for updates

Citation: Li, P.; Li, Q.; Feng, Q.; Huang, Z.; Gan, X.; Ding, H.; Xu, C. Multi-Source Monitoring and Numerical Simulation Deformation on Highway Steep Slopes Under Rainfall Effects. *Buildings* **2024**, *14*, 3473. https://doi.org/10.3390/buildings14113473

Academic Editor: Eugeniusz Koda

Received: 8 October 2024
Revised: 28 October 2024
Accepted: 28 October 2024
Published: 30 October 2024

Copyright: © 2024 by the authors. Licensee MDPI, Basel, Switzerland. This article is an open access article distributed under the terms and conditions of the Creative Commons Attribution (CC BY) license (https://creativecommons.org/licenses/by/4.0/).

1. Introduction

Landslides caused by rainfall represent a significant global natural disaster and often inflict damage on construction and transportation infrastructure [1–4]. In China, the rapid development of high-speed highways and railroads in mountainous areas has resulted in numerous unstable high and steep slopes adjacent to these routes, which are prone to landslides and rockfalls that pose threats to transportation and incur substantial annual losses [5–8]. Since the 1950s, the importance of slope stability evaluation has been recognized by numerous scientists and engineers in mitigating the risks associated with landslides. Theoretical methods for calculating slope stability safety factors include the Swedish arc method, the simple fabric method, the bar division method, and the Bishop's method [9–11]. These safety factors serve as criteria for determining slope stability. With advancements in computer technology, many scholars have adopted finite-element methods (the limit equilibrium method and strength reduction method) for slope stability analysis [12–15]. Furthermore, researchers have enhanced the classical method to account for factors such as rainfall and overloading in slope stability assessments [16–20]. However, the mechanisms underlying slope instability are complex, and many of these methods are static analyses, leading to significant discrepancies with actual conditions. Therefore, in-situ monitoring of slopes has emerged as one of the most effective approaches for assessing slope stability [21,22].

Traditional monitoring programs predominantly rely on manual methods that do not facilitate real-time monitoring [23] and are significantly influenced by environmental factors and monitoring frequency, resulting in delayed data that inadequately capture real-time deformation and fail to effectively predict landslide occurrences. The continuous development of sensor technology has led to the gradual implementation of innovative monitoring tools and techniques for slope monitoring. These include the use of MEMS technology for long-term monitoring of slope bodies [24], fiber-optic grating (FBG) vector displacement sensors for measuring slope vector displacement [25,26], as well as GPS and GNSS for deformation monitoring and early warning systems [27–31]. These methodologies have been theoretically and empirically validated by numerous scholars [32–36] and are now widely employed in various slope projects, with successful outcomes.

Currently, the monitoring approaches employed in slopes are relatively singular and lack the capability for multi-source monitoring and integrated data analysis. Most analyses are limited to the examination of monitoring data without incorporating numerical simulations for further insights. This paper focuses the critical slopes along the entire Yunmao Expressway, where the representative work sites of the project were selected. The study employed a combination of an early warning monitoring system (OTDR-distributed fiber-optic monitoring) and a quantitative deformation monitoring system (BeiDou system surface displacement monitoring and deep displacement monitoring) to establish a comprehensive multi-source monitoring scheme for slope stability assessment. The Geo Studio finite-element software was utilized for numerical simulation to systematically analyze the slope safety factor under different rainfall conditions and anti-slip pile configurations, aiming to provide guidance for practical applications.

2. Monitoring Methodology and Project Overview

2.1. Project Overview

The Yunmao Expressway that connects Yunfu Luoding and Maoming Xinyi (referred to as the Yunmao Expressway) is part of Guangdong Province's highway network planning of the "48 Union" project. According to the geological survey report, The highway traverses southwest, where the northern section passes through the Luoding Basin for strategically avoiding arable land by routing along the edge of the basin corner of the mountain slopes. The middle section crosses the Yunkai Mountain, which is characterized by complex terrain and geology as well as numerous high slopes. The southern section approaches the edge of the Xinyi Basin, where high slopes are less prevalent. The geological strata consists of recent polymictic sandstone, chert, metamorphic sandstone, mudstone, and some schist in the northern section, while the middle section primarily comprises metamorphic sandstone, mudstone, and granite. The southern section features metamorphic sandstone and mixed rock. The rock mass, influenced by folds and faults with a predominant northeast orientation, is fragmented and weathered to considerable depths. Coupled with high rainfall, this results in poor slope stability.

The route of the Yunmao Expressway predominantly employs deep excavation graben and high-fill embankment, with 73 graben slopes exceeding 40 m in height and over 10 embankment slopes exceeding 35 m along the entire route. Notably, the highest road graben slope is located on the left slope of K61 + 230 to K61 + 380, with a maximum slope height of 61 m. The highest embankment slope is situated on the left embankment slope of K68 + 010 to K68 + 220, with a maximum thickness of 60 m.

The complexity of slope structures, compounded by the number and height of slopes along the Yunmao Expressway, necessitates corresponding protective and reinforcement measures during construction to maintain overall slope stability and safety. Nevertheless, under extreme meteorological conditions or adverse circumstances, the occurrence of localized slope instability or damage remains a possibility, which may affect highway operations, traffic flow, and safety. In severe case, such events could lead to significant accidents, including collapses, road damages, vehicle destruction, and fatalities, which may result in considerable economic losses. Therefore, comprehensive monitoring and early

warning measures for roadway slopes are essential, with an emphasis on expanding the scope of monitoring and control coverage, particularly for key complex, deep excavation and high-fill slopes.

2.2. Monitoring Program

This study focused on the key complex high slopes within the designated road section, specifically targeting high-road graben slopes exceeding 45 m, steep embankment slopes exceeding 20 m, and critical slopes that experienced landslide damage during the construction period. A total of 53 locations were monitored. Some monitoring projects are shown in Table 1.

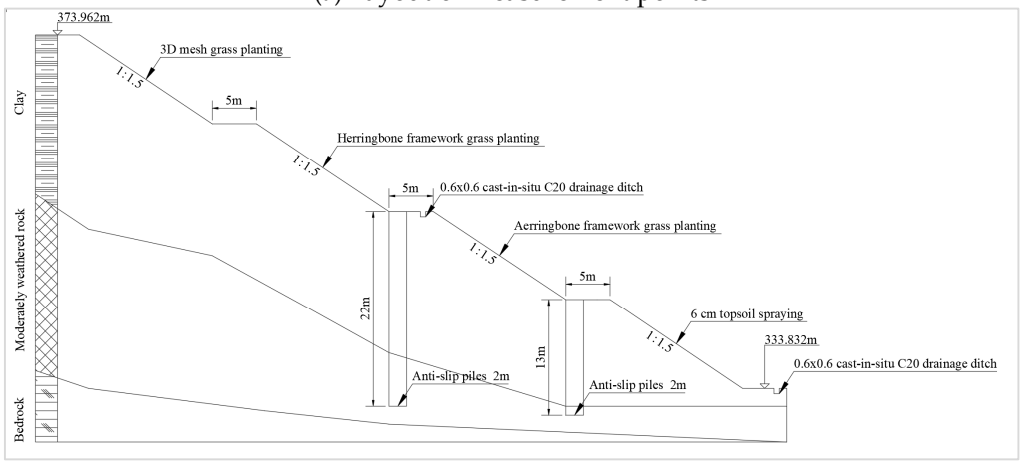
Table 1. Some key slope monitoring items of Yunmao Expressway.

No.	Section	Placement	Monitoring Program
1	Pingtang interchange K44 + 515-K44 + 645	Left side	OTDR-distributed fiber monitoring
2	K49 + 065-K49 + 420	Right side	OTDR-distributed fiber monitoring and quantitative deformation monitoring systems (horizontal displacement monitoring at the top of anti-slip piles, deep horizontal displacement monitoring, and precipitation monitoring)
3	Pingtang service area K49 + 875-K50 + 110	Right side	OTDR distributed fiber monitoring

This study focused on the section from K49 + 065 to K49 + 420 (as shown in Figure 1). The slope is a four-tier slope (with each tier being 10 m high) and is equipped with anti-slide piles (the pile bodies are made of C30 concrete with a diameter of 2 m), anchor cable frames, and soil spray vegetation protection. GKYL-92 integrated piezoelectric rain gauges were positioned on the secondary platform of the slope, while array displacement gauges were installed at the secondary platform of the slope, the tertiary slope, and the top of the rift valley. Additionally, MIS30 pervasive dual-frequency-integrated GNSS receivers were deployed on the secondary platform of the slope, and OTDR-distributed fiber-optic monitoring stations were systematically arranged along the slope. Each slope within the designated road section was equipped with a light source signal demodulation equipment monitoring sub-station, which connects the signal demodulation equipment to the buried monitoring fiber optic. The monitoring sub-station data were collected through a wireless network to the server by the system, where a total of three sensors were integrated to enable the acquisition of real-time deformation data and precipitation conditions. Monitoring commenced on 13 December 2022. Due to the extensive distribution of measurement points and data, this paper selectively analyzes typical data, and the specific layout and installation-effect diagram are displayed in Figure 1.



(**a**) Layout of measurement points



(**b**) Section A-A schematic diagram



(**c**) Installation diagram of measurement points

Figure 1. Layout of measurement points in section from K49 + 065 to K49 + 420 of Yunmao Expressway.

3. Typical Monitoring Data

3.1. Analysis of the Effect of Rainfall on Slope Displacement

Guangdong Province, characterized as a typical coastal city with a subtropical monsoon climate, experiences low rainfall levels at the beginning of the year, which significantly increases during the summer months [37]. Analyzing the 2023 rainfall monitoring data, as depicted in Figure 2, reveals that monthly rainfall from January to June is markedly lower than that from June to December. Rainfall escalates rapidly from June and reaches a maximum monthly rainfall of 1328.1 mm in September. The subsequent sections analyze the rainfall pattern, deep slope deformations, and displacements at the tops of skidding piles during the latter half of 2023.

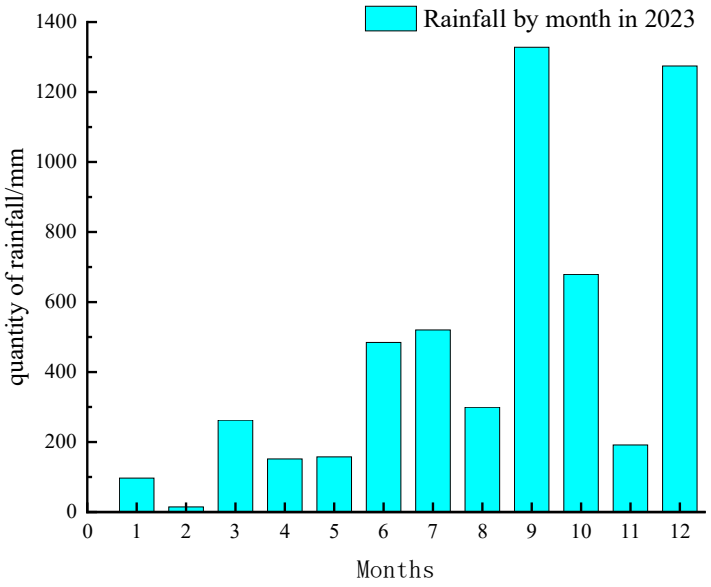


Figure 2. Rainfalls in the year 2023.

3.2. Analysis of Horizontal Displacements at Different Depths of Slopes

For the right-side slope in the section from K49 + 065 to K49 + 420, array displacement meters were deployed at K49 + 175, K49 + 260, K49 + 270, and K49 + 330, respectively. The x-axis of the displacement meter aligns with the direction of the slope, while the y-axis is parallel to the highway. The specific deployment details are presented in Table 2. The effect of rainfall infiltration on slope stability is a gradual process, and to ensure the accuracy of the data, the monitoring platform collects data on rainfall and deformation every 30 min and retrieves the monitoring data from four measurement points. Displacement data in the x-axis direction at a depth of 1 m and daily rainfall from June to December were extracted, with results illustrated in Figure 3.

Table 2. Deployment information for depth horizontal displacement monitoring.

Placement	Section	Depth of Measurement Point
Secondary platforms	K49 + 270	24 m
Secondary platforms	K49 + 330	32 m
Three-level platform	K49 + 215	26 m
Moat top, rift valley	K49 + 260	41 m

Due to damage to the array displacement meter at K49 + 330, it was replaced on August 16, followed by a displacement zeroing operation. As observed in Figure 3, four significant rainfall events occurred on 17 July, 2 September, 20 October, and 23 December, with rainfall amounts exceeding 200 mm/day. With the occurrence of rainfall, The displacement in the x-axis direction at a depth of 1 m increased rapidly with rainfall, exhibiting some hysteresis, which is consistent with previous research findings.

Among the four measurement points at the top of the rift valley, secondary platform, and tertiary platform, the top of the rift valley exhibited the largest displacement, while the tertiary platform displayed smaller displacement than the top of the rift valley yet larger than that of the secondary platform. Given that the monitored slope is a Class IV slope, the displacement in the mid-slope was approximately half that at the top of the rift valley.

Consequently, the top of the rift valley emerged as a critical point of concern after rainfall, which requires focused monitoring of its displacement to further analyze the underlying deformation and causes.

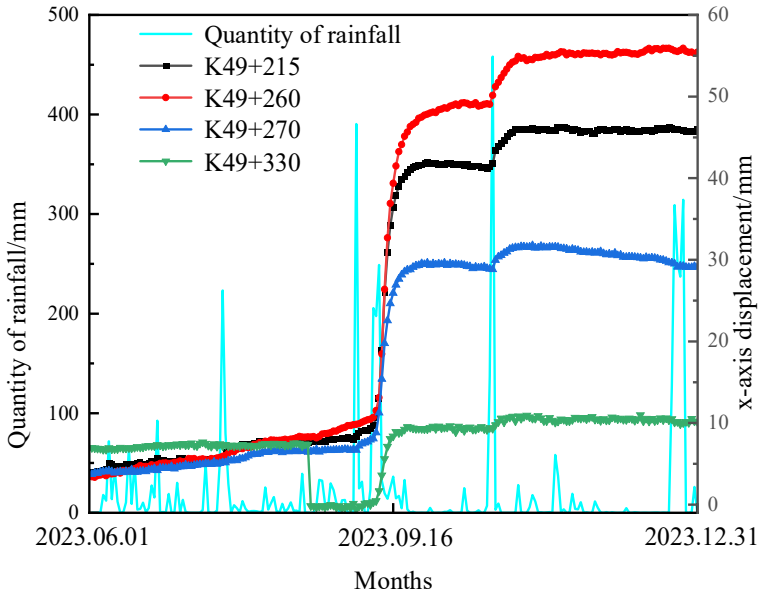


Figure 3. Displacement in the x-axis direction at a depth of 1 m and rainfall at each measurement point.

Figure 3 indicates that concentrated rainfall occurred prior to the first significant rainfall event; however, all preceding rainfall was relatively minor, leading to gradual slope deformation. In contrast, the second significant rainfall event was preceded and followed by prolonged concentrated rainfall, resulting in a sharp increase in slope displacement. Although the third rainfall event did not appear entail concentrated rainfall, it recorded a single-day total of 458.1 mm, which corresponded with minor displacement. The fourth rainfall event did not entail concentrated rainfall, so it did not significantly impact the slope stability. Thus, the necessary conditions for triggering slope instability include both the duration of rainfall and the cumulative rainfall amount reaching a certain threshold.

3.3. Top Displacement of the Anti-Slip Pile

The collection frequency for each measurement point was set at every half hour. As illustrated in Figure 3, concentrated heavy rainfall occurred from 2 September to 20 September. Monitoring data for the top displacement of anti-slip piles at both the primary and secondary platforms were extracted for the period from 6 September to 19 September, and the results are depicted in Figure 4. The data indicate a sharp increase in the top displacements of the anti-slip piles at the secondary platform on 9 September, and the deformation stabilized on 18 September, with a displacement offset of 6.65 mm towards the critical surface of the slope. The surface layer displacement at the secondary platform reached 9 mm, as shown in Figure 5b. Following rainfall infiltration, the weight of the slope increased, which surpassed the slip resistance, resulting in sliding displacement. The sliding soil exerted forces on the anti-slip piles. The presence of anti-slip piles and other reinforcement measures significantly enhanced the slope's resistance to sliding and mitigated the further deformation. The primary platform, which is located at the corner of the slope and near the water table, possessed soil with a high water content prior to rainfall. After rainfall began, the rainfall infiltration was minimal, with most water discharged as runoff. Consequently, the un-displaced piles at the primary platform remained stable throughout the monitoring cycle, which suggests that the deformation area was primarily concentrated in the upper part of the slope, while the lower part remained stable.

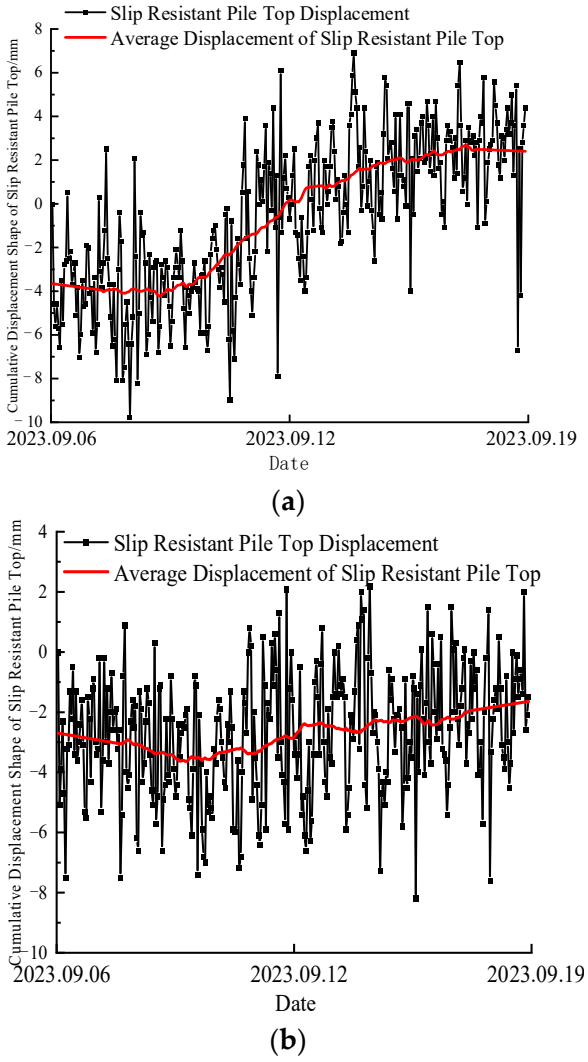


Figure 4. Cumulative top displacement of the anti-slip piles. (**a**) Cumulative top displacement of the anti-slip pile on secondary platform; (**b**) cumulative top displacement of the anti-slip pile on the primary platform.

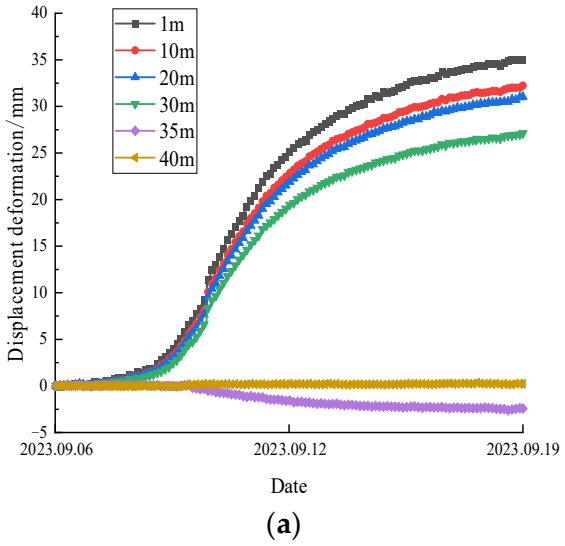


Figure 5. *Cont.*

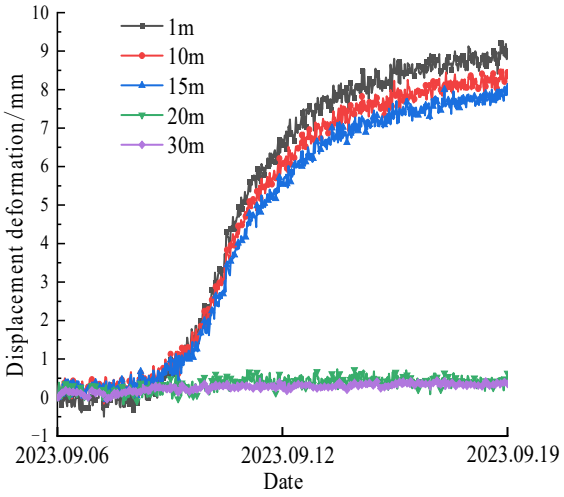


Figure 5. Time-dependent displacements of the rift top and secondary platform at different depths. (**a**) Time-dependent displacements at the top of the rift valley at different depths; (**b**) time-dependent displacements of the secondary platform at different depths.

3.4. Analysis of Measured Slope Displacement

The monitoring data from the top of the rift valley at section K49 + 260 and the secondary platform at section K49 + 330 reveal that slope displacement increased rapidly during the 14-day interval from 6 September to 15 September. Deformation curves at different depths for the two measurement points are presented in Figure 5. The data from both monitoring points indicate that the slope underwent three distinct deformation stages during the monitoring cycle: an initial stage characterized by stability with minimal deformation, a middle stage of rapid displacement and deformation, and a late stage where deformation gradually slowed and approached stabilization.

Figure 5 illustrates that slope displacement surged abruptly from 10 September to 14 September, with a total deformation of 27.782 mm at the top of the rift valley and 8.075 mm at the secondary platform over the four-day observation period. Analysis of the deformation curves in Figure 5a,b shows that slope deformation at the top of the rift valley decreases gradually from 0 m to 30 m, followed by a rapid decrease beyond that depth. Similarly, slope deformation at the secondary platform decreased gradually from 0 m to 15 m before declining sharply thereafter. This suggests that the sliding surface of the slope is positioned at a depth of approximately 35 m, with the transition from significant to minor deformation occurring between 30 m and 35 m.

The deformation trend of the slope aligns with the displacement observed at the top of the anti-slip piles at the secondary platform. The x-direction displacement at the top of the secondary platform was less than that at the top of the rift valley at a depth of 20 m, which indicates that the anti-slip piles effectively mitigate further deformation of the slope body.

To investigate the long-term deformation evolution of the slope, monitoring data from the secondary platform at sections K49 + 260 and K49 + 330 (hereafter referred to as the first and second sections, respectively) were analyzed to examine the relationship between deformation and depth. As illustrated in Figure 6, two primary inflection points were identified across different monitoring sections during any monitoring period: the first inflection point occurred at approximately 35 m from the slope top (17 m deep from the secondary platform), where slope displacement decreased rapidly. The second inflection point was located at nearly 35 m deep (17 m deep from the secondary platform), where the slope displacement at depths below this point remained relatively stable within a specific range.

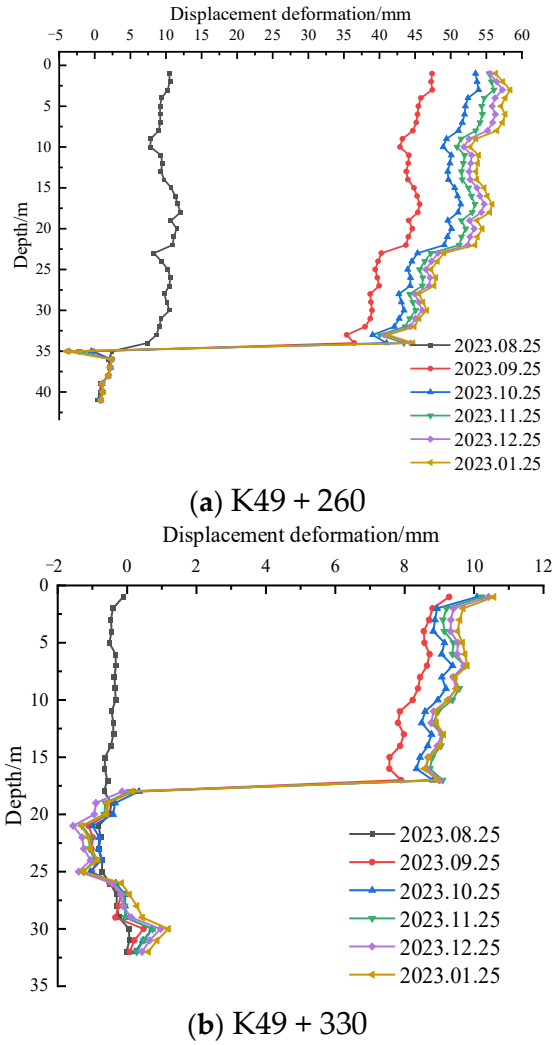


Figure 6. Relationship between deformation and cross-sectional depth of the slopes.

It is evident from Figure 6 that the rainfall from 25 August to 25 September did not significantly impact the slope displacement, but minimal displacements were observed during subsequent rainfall events, indicating that the slope remained largely stable. Within a 35 m depth above the first section, slope displacement decreased slowly with increasing depth, with the 20 m depth serving as a demarcation point. This was attributed to the presence of anti-slip piles and other reinforcement measures at this depth, which resulted in a smaller rate of change in slope deformation compared to the 20 m to 35 m depth range.

The deformation inflection points for the first and second sections were situated at burial depths of 35 m and 37 m, respectively. Below these inflection points, the displacements of the slope body were minimal and did not exhibit abrupt changes, which indicates that the potential slip surface of the slope was between burial depths of 35 m and 37 m. This conclusion aligns with the findings presented in Figure 5.

Subsequently, numerical simulations on slope stability were performed to facilitate a simplified analysis of slope behavior and reveal change patterns under varying rainfall conditions. This was anticipated to provide valuable insights for practical applications.

4. Numerical Simulation

4.1. Establishment of the Slope Model

The slopes at the Section A-A in Figure 1a are characterized as graben slopes composed of uniform soils. The strata at the site are divided into three layers from top to bottom: clay, fully weathered rock, and hard rock. The simulated slope is a four-level structure with a

height of 50 m, where each level is 10 m high and 5 m wide, resulting in a total slope width of 85 m and a gradient of 1:1.5. The slope model and meshing are depicted in Figure 7. Anti-slip piles were incorporated at both the primary and secondary platforms, with the water table line positioned at 13 m on the left and 5 m on the right. The size of the divided mesh was set to 1 m. All meshes were quadrilateral and triangular, resulting in a total of 2617 nodes and 2519 elements.

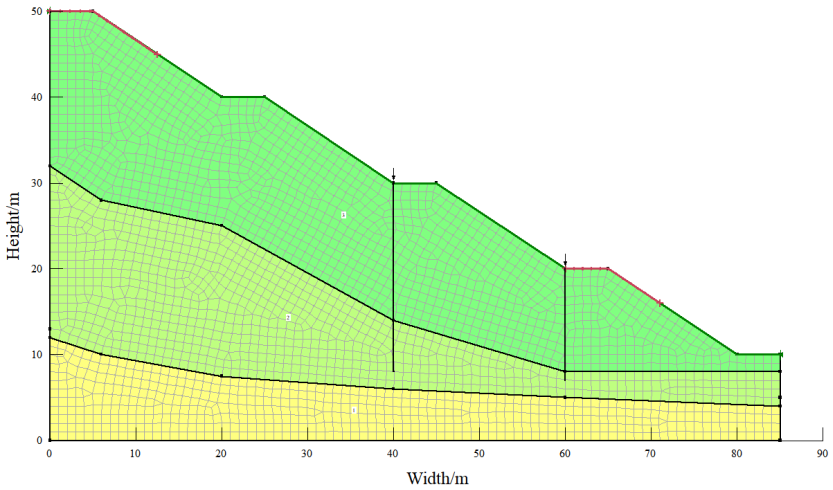


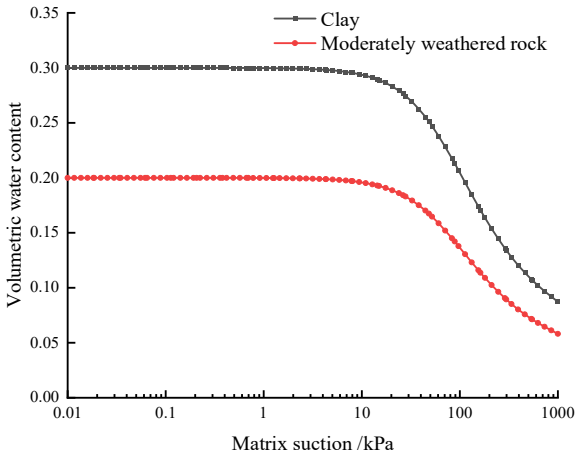
Figure 7. Schematic diagram of slope model and meshing.

4.2. Selection of Parameters

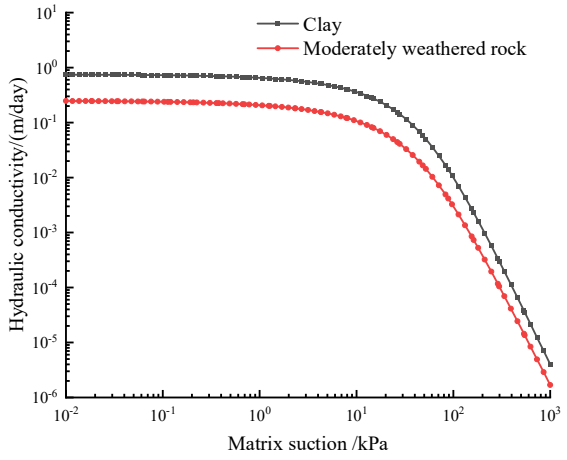
In this study, rainfall seepage analysis of slopes was conducted using the limit equilibrium modules SEEP/W and SLOPE/W in Geo Studio finite-element software, and the Morgenstern–Price method was selected for slope stability analysis in SEEP/W. The material parameters for the slope are presented in Table 3 and Figure 8. Given the heterogeneous nature of slope soil in the real working condition, with suboptimal rainfall infiltration influenced by various factors, such as rainfall conditions, slope water volume, and water drainage, etc., several assumptions were made to simplify calculations and highlight the study's focus. The slopes were assumed to be isotropic and homogeneous materials; evapotranspiration was not considered during the study period, water did not pool on the slope surface, and precipitation that failed to infiltrate was discharged as surface runoff.

Table 3. Physical and mechanical parameters of slope materials.

Slope Materials	Material Model	Gravity /(kN·m^{-3})	Cohesion/kPa	Internal Friction Angle/(°)	Saturated Permeability Coefficient K_s (m·d^{-1})
Clay	Saturated/unsaturated	18.4	22	9	0.75
Moderately weathered rock	Saturated/unsaturated	20.4	35	19	0.25
Bedrock	Saturated	30	3.1×10^4	54	0.191



(**a**) Soil Water Characteristic Curve



(**b**) Permeability Curve

Figure 8. Soil Water Characteristic Curve (SWCC) and Permeability Curves for Each Geotechnical Layer of the Slope.

4.3. Settings for Rainfall and Monitoring Programs

This study examined the effects of different rainfall conditions on slope stability by analyzing changes in the slope safety factor, location of the slip surface, and pore water pressure governed by rainfall intensity and duration.

According to the National Weather Service, rainfall intensity is categorized based on the amount of precipitation over a 24-h period: light rain (0.1–9.9 mm), moderate rain (10–24.9 mm), heavy rain (25–49.9 mm), very heavy rain (50–99.9 mm), extremely heavy rain (100–249.9 mm), and exceptionally heavy rain ($\geq$250 mm). Rainfall monitoring records from the Dependent Project indicate that from June to December 2023, there were 5 or more days of exceptionally heavy rainfall, 7 days of heavy rainfall, 6 days of torrential rainfall, 19 days of heavy rainfall, and 177 days of light to moderate rainfall. During light and moderate rainfall conditions, the slope could quickly discharge rainwater without significantly affecting the slope stability; thus, this study focused solely on heavy or greater rainfall when establishing rainfall conditions. The rainfall intensity was set at 50 mm/day, with durations of 1, 2, and 3 days. A total analysis time of 7 days was considered, including changes occurring 4 days after rainfall.

4.3.1. Effect of Rainfall Duration on Slope Stability

Figure 9 illustrates that as the rainfall duration increased, the slope safety factor experienced greater changes. In the early stage, the magnitude of change in the slope safety factor remained consistent; however, longer durations required more time for recovery

after rainfall cessation. At the onset of rainfall, the slope body was in a dry state, while the surface soil absorbed water and became heavier. This action on the slope body was equivalent to exerting a circumferential pressure on the internal soil body, so there was a transient increase in the slope safety factor. The rapid displacement changes observed in the preceding section exhibited a certain lag relative to the onset of rainfall, which is consistent with the measured results. Following sustained rainfall, the infiltration led to saturation in the shallow layer of the slope body, which resulted in increased slope weight and decreased slip resistance, so the safety factor continued to decrease.

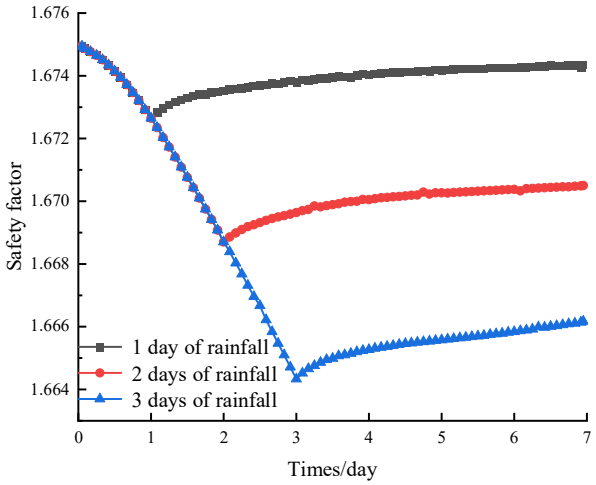


Figure 9. Variation of slope safety factor at different calendar times at a rainfall intensity of 50 mm/d.

After rainfall cessation, the slope safety factor did not recover immediately; rather, it experienced a slight decrease for a period as the internal water continued to infiltrate and seep into the groundwater. In the absence of additional rainfall, the pore water pressure dissipated, reducing weight and enhancing shear strength, which allowed the safety factor to gradually recover at a decreasing rate. However, it did not return to the initial condition, which indicates that rainfall has a prolonged negative effect on slope stability.

Figure 10 depicts the location of the potential slip surface of the slope. It reveals that the deepest part of the potential slip surface lies beneath the secondary platform and is 37 m away from the slope top. This finding corroborates the earlier measured potential slip surface identified at a depth of 35 m to 37 m in the deformation analysis presented in Section 3.4.

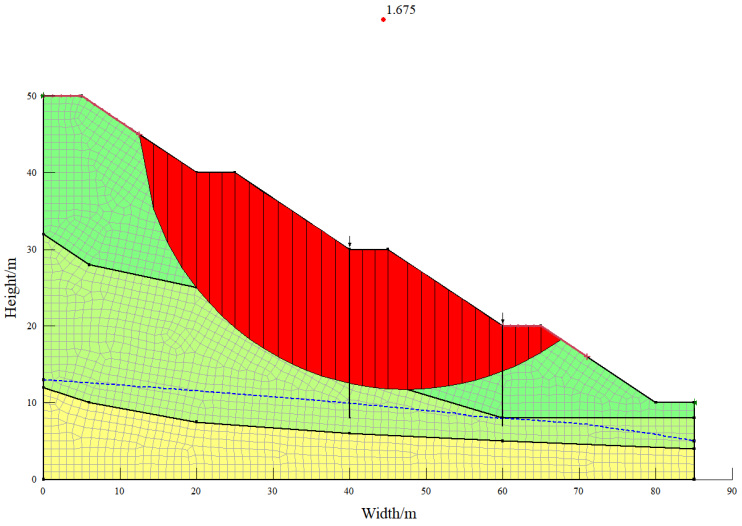


Figure 10. Potential slip surfaces on slopes.

4.3.2. Effect of Different Rainfall Conditions on Slope Stability

This subsection primarily analyzes the effect of different rainfall intensity and duration on slope stability under identical total rainfall conditions,. Three simulation scenarios were established: rainfall intensity of 60 mm/day for 6 days, rainfall intensity of 90 mm/day for 4 days, and rainfall intensity of 180 mm/day for 2 days. The trend of changes in slope stability factor over time under these three scenarios was examined.

As illustrated in Figure 11, for a given amount of rainfall, the greater the rainfall intensity, the greater the decrease in the slope safety factor, and the greater the magnitude of change. With increased rainfall intensity, the volume of slope runoff rose, while the infiltration volume was smaller than that under the low-intensity rainfall condition. Therefore, the recovery rate of the safety factor under the high-intensity rainfall condition was quicker than that under the low-intensity rainfall condition. A prolonged period of low-intensity rainfall facilitated greater infiltration. Consequently, the safety factor was restored immediately after the cessation of rainfall, but it remained low for a period of time before returning to a higher level. These observations align with the monitoring results from previous section, where the slope displacement under short-term, heavy rainfall conditions fluctuated within a narrow range, and the impact on the slope was smaller than that of long-term rainfall with heavy rainfall conditions. Therefore, in the actual project, enhanced monitoring of slopes and the implementation of contingency measures for the long-term heavy rainfall events are warranted.

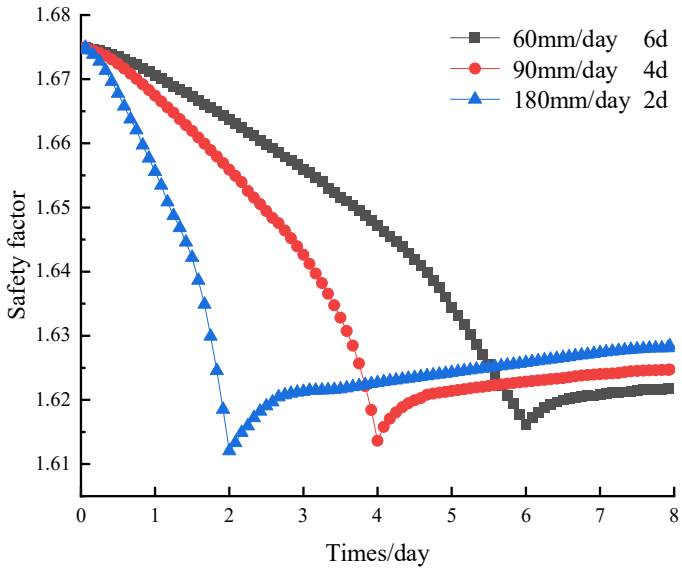
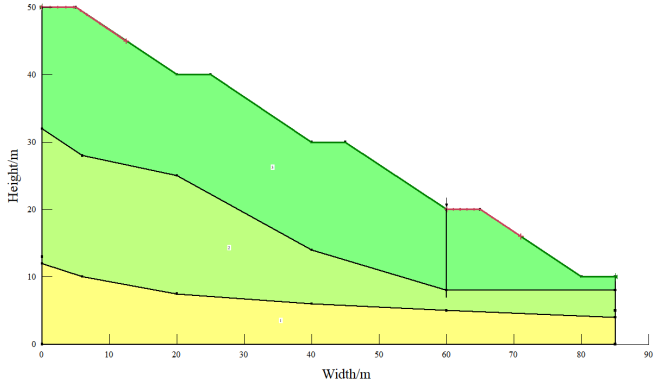


Figure 11. Variation of slope safety factor under different rainfall conditions.

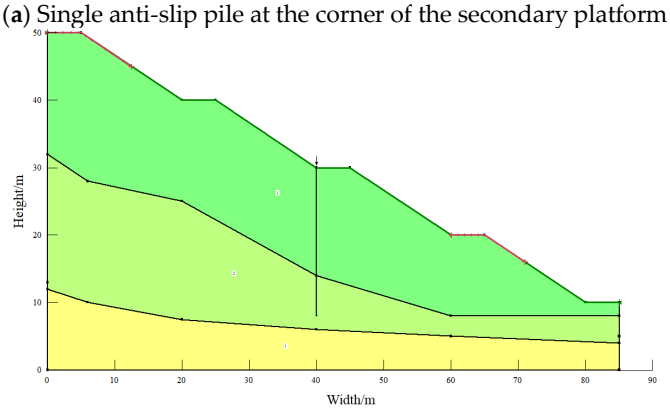
4.4. Effect of Anti-Slip Piles on Slope Stability

4.4.1. Effect of Different Locations of Anti-Slip Piles

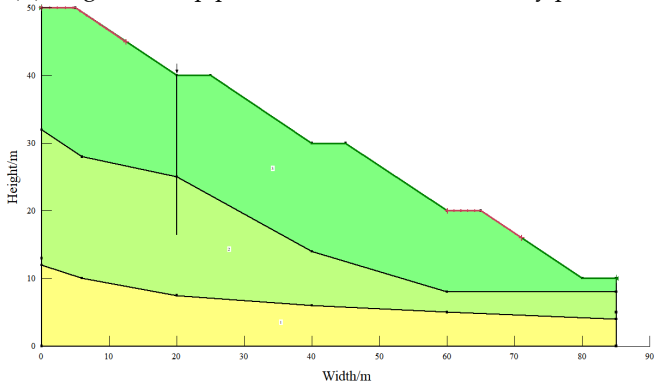
The location and number of anti-slip piles on the slope were varied to study the effect of different anti-slip pile configurations on slope stability. When only a single anti-slip pile was installed on the slope under a rainfall condition of 50 mm/day for 3 days, four different scenarios were established: a single anti-slip pile at the corner of the secondary platform, a single anti-slip pile at the corner of the tertiary platform, a single anti-slip pile at the corner of the Class IV platform, and without an anti-slip pile, as shown in Figure 12.



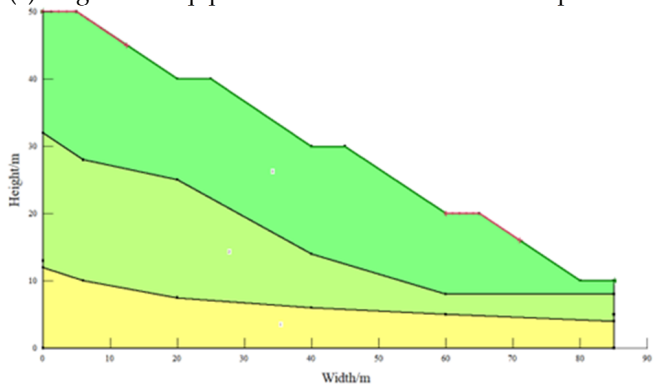
(**a**) Single anti-slip pile at the corner of the secondary platform



(**b**) Single anti-slip pile at the corner of the tertiary platform



(**c**) Single anti-slip pile at the corner of the Class IV platform



(**d**) Without anti-slip pile

Figure 12. Different layouts of single anti-slip pile.

The safety factors under these four scenarios are presented in Table 4. The magnitudes of changes in slope stability factor before and after rainfall were basically consistent across

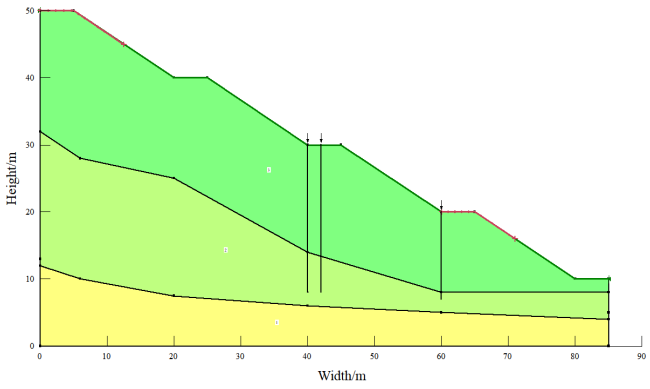
all scenarios, and the initial stability factor for scenarios with anti-slip piles were higher than that without an anti-slip pile. The lower the location of the anti-slip piles, the higher the safety factor. When the anti-slip piles were positioned at the corner of the secondary platform, the safety factor was significantly increased. As previously noted, the landslide cracking surface was above the corner of the secondary platform, which indicated that anti-slip piles above this platform could only counteract lateral sliding force for a portion of the slope. Therefore, considerable soil mass may continue to be displaced downward, while the sliding force of the slope continues to be reduced. Anti-slip piles at the secondary platform effectively prevented most slope soil from further deformation and displacement, thus enhancing the slope safety factor. Therefore, in practical applications, priority should be given to placing anti-slip piles at lower slope elevations.

Table 4. Variation of stability factor for different layouts of single anti-slip pile.

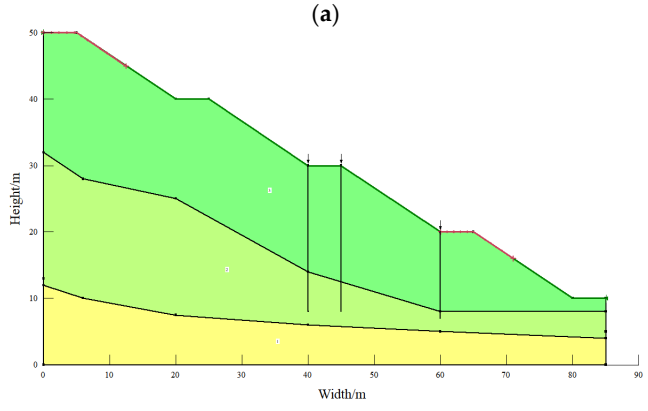
Location of Anti-Slip Piles	Initial Safety Factor	After the Rainfall Exceeds the Safety Margin	Difference in Safety Factor
Without anti-slip piles	1.127	1.118	0.009
At the corner of Class IV platform	1.642	1.633	0.009
At the corner of the tertiary platform	1.647	1.638	0.009
At the corner of the secondary platform	1.652	1.641	0.009

4.4.2. Effect of Different Spacing of Anti-Slip Piles

Double-row piles with spacing of 2.5 m and 5 m were arranged at the slope secondary platform and tertiary platform, respectively, under the same rainfall condition of 50 mm/day for 3 days. The layout of anti-slip piles is illustrated in Figure 13.

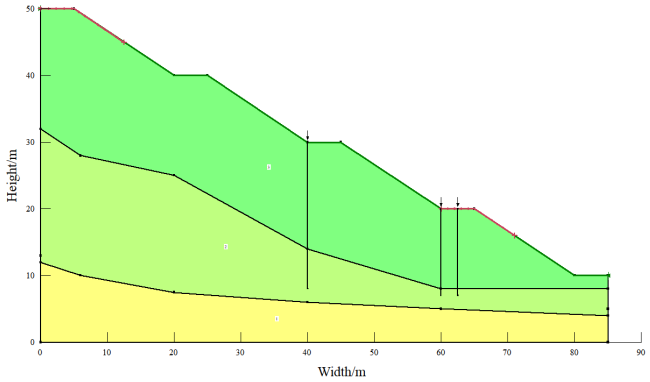


(**a**)

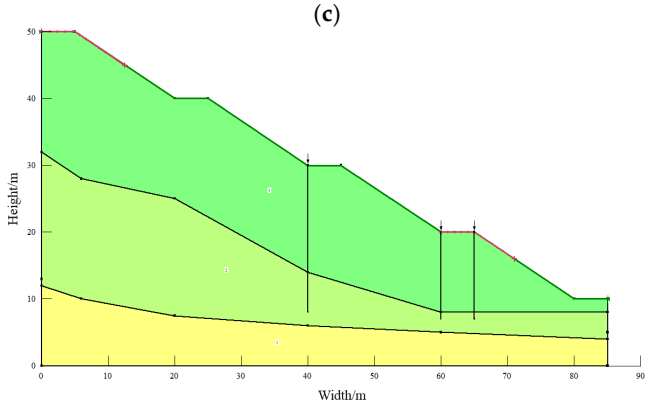


(**b**)

Figure 13. *Cont.*



(**c**)



(**d**)

Figure 13. Layouts of double-row anti-slip piles with different spacing at different locations. (**a**) Double-row anti-slip piles with a spacing of 2.5 m at the corner of the tertiary platform; (**b**) double-row anti-slip piles with a spacing of 5 m at the corner of the tertiary platform; (**c**) double-row anti-slip piles with a spacing of 2.5 m at the corner of the secondary platform; (**d**) double-row anti-slip piles with a spacing of 5 m at the corner of the secondary platform.

The stability factors for these four different scenarios are presented in Table 5, which reveals that the magnitudes of changes in the stability factor before and after rainfall were basically consistent across all scenarios. The initial stability factor across various scenarios was comparable; however, the initial safety factor of 1.127 under the original scenario was increased by approximately 51%. Compared with the deployment of a single anti-slip pile, this arrangement improved the safety factor by about 3%. Nonetheless, given that the slope was already in a stable state, practical considerations such as budget constraints and project timelines should inform optimal decision making.

Table 5. Variation of stability factor for different locations with different spacing of anti-slip piles.

Location and Spacing of Anti-Slip Piles	Initial Safety Factor	After the Rainfall Exceeds the Safety Margin	Difference in Safety Factor
At the corner of the tertiary platform at 2.5 m intervals	1.699	1.688	0.011
At the corner of the tertiary platform at 5 m intervals	1.699	1.688	0.011
At the corner of the secondary platform at 2.5 m intervals	1.702	1.690	0.012
At the corner of the secondary platform at 5 m intervals	1.702	1.691	0.011

5. Discussion

This study conducted a stability analysis of the slopes along the Yunmao Expressway. It also verified the previously proposed observation that slope deformation exhibits a significant lag in response to rainfall, and not every rainfall event results in large displacements or landslides, but rather, significant slope deformation or instability occurs only when rainfall exceeds a certain threshold [38]. The use of anti-slide piles in the slopes can greatly enhance stability; however, geological conditions may vary significantly in different landslide-prone areas [39]. This study aimed to provide some reference for the arrangement of anti-slide piles along the slopes of the Yunmao Expressway. In practical engineering, the collected rainfall data can effectively quantify the levels of previous rainfall, which can be used in conjunction with later weather forecasts to verify whether these values will exceed the rainfall threshold. By integrating data from various monitoring points, a multi-source early warning platform can be developed to issue different levels of alerts for unstable slopes, which is crucial for reducing human casualties and landslide risks.

6. Conclusions

This study analyzed slope sliding and cracking behavior based on the monitoring data from the actual project. It was demonstrated that reinforcement measures such as anti-slip piles can significantly enhance slope stability. Additionally, numerical simulations were conducted to investigate slope stability under different rainfall conditions.

(1) Short-term heavy rainfall had a minimal impact on slope deformation; however, extensive concentrated heavy rainfall could lead to dramatic increases in slope displacement, with a certain hysteresis. There was a rainfall threshold required to induce significant deformation;

(2) Under identical scenarios, the deformation at the top of the rift valley at a depth of 20 m was greater than that at the top of the secondary platform. The deformation rate of the slope below the deployment of anti-slip piles was greater than that of the position above them. The deformation primarily concentrated in the middle and upper parts of the slope, while the lower part remained stable. The potential slip surface was located at a depth of 35 m to 37 m and remained almost unchanged throughout the monitoring cycle. The slope above the potential slip surface stabilized progressively after experiencing significant deformation, and then, a new stable equilibrium state was established;

(3) Numerical simulation results indicated that the deepest slope slip surface was situated at a depth 37 m from the slope top and was beneath the secondary platform, which validated the arrangement of monitoring points and the effectiveness of the detection program. The actual project should prioritize monitoring deformation in the middle and upper parts of the slope, especially during long-term rainfall events accompanied by intense rainfall, as these conditions substantially affect slope stability;

(4) The presence and location of anti-slip piles significantly influenced slope stability. Anti-slip piles positioned in the lower part of the slope exerted a more substantial positive effect on the slope stability, while double-row piles could also markedly enhance slope stability. However, this gain effect was independent of the spacing in this case. Practical considerations including project budget, construction timelines, and other issues should guide optimal pile-placement decisions.

Author Contributions: Conceptualization, P.L. and H.D.; Methodology, Q.L.; Software, C.X.; Validation, Z.H.; Formal analysis, X.G.; Investigation, Q.L. and Z.H.; Resources, Q.L., H.D. and C.X.; Data curation, P.L., Q.F., Z.H. and H.D.; Writing—original draft, X.G.; Writing—review & editing, X.G.; Visualization, Q.F.; Supervision, C.X.; Project administration, P.L. All authors have read and agreed to the published version of the manuscript.

Funding: This research received no external funding.

Data Availability Statement: Data is unavailable due to privacy.

Conflicts of Interest: Authors Peijun Li, Qing Li, Qingshan Feng and Zhendong Huang were employed by Guangdong Jiaoke Testing Co., Ltd. All authors declare no conflicts of interest.

References

1. Zhao, B.; Su, L.; Xu, Q.; Li, W.; Xu, C.; Wang, Y. A review of recent earthquake-induced landslides on the Tibetan Plateau. *Earth-Sci. Rev.* **2023**, *244*, 104534. [CrossRef]
2. Gariano, S.L.; Guzzetti, F. Landslides in a changing climate. *Earth-Sci. Rev.* **2016**, *162*, 227–252. [CrossRef]
3. Pereira, S.; Zêzere, J.L.; Quaresma, I.D.; Bateira, C. Landslide incidence in the North of Portugal: Analysis of a historical landslide database based on press releases and technical reports. *Geomorphology* **2014**, *214*, 514–525. [CrossRef]
4. Zhang, Y.; Tang, J.; Liao, R.; Zhang, M.F.; Zhang, Y.; Wang, X.M.; Su, Z.Y. Application of an enhanced BP neural network model with water cycle algorithm on landslide prediction. *Stoch. Environ. Res. Risk Assess.* **2021**, *35*, 1273–1291. [CrossRef]
5. Zhang, W.; Zhao, X.; Pan, X.; Wei, M.; Yan, J.; Chen, J. Characterization of high and steep slopes and 3D rockfall statistical kinematic analysis for Kangyuqu area, China. *Eng. Geol.* **2022**, *308*, 106807. [CrossRef]
6. Ji, Z.M.; Chen, T.L.; Wu, F.Q.; Li, Z.H.; Niu, Q.H.; Wang, K.Y. Assessment and prevention on the potential rockfall hazard of high-steep rock slope: A case study of Zhongyuntai mountain in Lianyungang, China. *Nat. Hazards* **2023**, *115*, 2117–2139. [CrossRef]
7. Zhou, F.; Liu, X.; Tang, H.; Miao, M.; Xu, B.; Guo, X. Analysis of the frequency–response stability and reliability of a tower-column unstable rock mass on a high and steep slope. *Sci. Rep.* **2024**, *14*, 20308. [CrossRef]
8. Ferrari, F.; Giacomini, A.; Thoeni, K.; Lambert, C. Qualitative evolving rockfall hazard assessment for highwalls. *Int. J. Rock Mech. Min. Sci.* **2017**, *98*, 88–101. [CrossRef]
9. Zhang, J.Y.; Wan, L.P.; Duan, G.Y. Study on sensitivity analysis method of slope stability based on Sweden arc method. *Curr. Sci.* **2017**, *113*, 2097–2104. [CrossRef]
10. Cai, F.; Ugai, K. Numerical analysis of rainfall effects on slope stability. *Int. J. Geomech.* **2004**, *4*, 69–78. [CrossRef]
11. Zhao, T.; Sun, J.; Zhang, B.; Li, C. Analysis of slope stability with dynamic overloading from earthquake. *J. Earth Sci.* **2012**, *23*, 285–296. [CrossRef]
12. Shin, J.W.; Baek, Y.; Song, J.H. Analysis of the Failure Area of the Slope Using the Slip Line Method. *Appl. Sci.* **2023**, *13*, 3863. [CrossRef]
13. Thiebes, B.; Bell, R.; Glade, T.; Jäger, S.; Anderson, M.; Holcombe, L. A WebGIS decision-support system for slope stability based on limit-equilibrium modelling. *Eng. Geol.* **2013**, *158*, 109–118. [CrossRef]
14. Leshchinsky, B.; Ambauen, S. Limit equilibrium and limit analysis: Comparison of benchmark slope stability problems. *J. Geotech. Geoenviron. Eng.* **2015**, *141*, 04015043. [CrossRef]
15. Liu, Z.; Shao, J.; Xu, W.; Chen, H.; Zhang, Y. An extreme learning machine approach for slope stability evaluation and prediction. *Nat. Hazards* **2014**, *73*, 787–804. [CrossRef]
16. Durukan, S. Evaluation of the Antecedent Saturation and Rainfall Conditions on the Slope Failure Mechanism Triggered by Rainfalls. *Appl. Sci.* **2024**, *14*, 9478. [CrossRef]
17. Liu, X.; Wang, Y. Probabilistic simulation of entire process of rainfall-induced landslides using random finite element and material point methods with hydro-mechanical coupling. *Comput. Geotech.* **2021**, *132*, 103989. [CrossRef]
18. Cuomo, S.; Di Perna, A.; Martinelli, M. Modelling the spatio-temporal evolution of a rainfall-induced retrogressive landslide in an unsaturated slope. *Eng. Geol.* **2021**, *294*, 106371. [CrossRef]
19. Zhou, J.; Qin, C. Finite-element upper-bound analysis of seismic slope stability considering pseudo-dynamic approach. *Comput. Geotech.* **2020**, *122*, 103530. [CrossRef]
20. Wang, W.; Yin, Y.; Zhu, S.; Wang, L.; Zhang, N.; Zhao, R. Investigation and numerical modeling of the overloading-induced catastrophic rockslide avalanche in Baige, Tibet, China. *Bull. Eng. Geol. Environ.* **2020**, *79*, 1765–1779. [CrossRef]
21. Xie, F.; Larose, E.; Wang, Q.; Zhang, Y. In-situ monitoring of rock slope destabilization with ambient seismic noise interferometry in southwest China. *Eng. Geol.* **2023**, *312*, 106922. [CrossRef]
22. Theocharis, A.I.; Zevgolis, I.E.; Deliveris, A.V.; Karametou, R.; Koukouzas, N.C. From climate conditions to the numerical slope stability analysis of surface coal mines. *Appl. Sci.* **2022**, *12*, 1538. [CrossRef]
23. Pei, H.; Zhang, S.; Borana, L.; Zhao, Y.; Yin, J. Slope stability analysis based on real-time displacement measurements. *Measurement* **2019**, *131*, 686–693. [CrossRef]
24. Barzegar, M.; Blanks, S.; Sainsbury, B.A.; Timms, W. MEMS technology and applications in geotechnical monitoring: A review. *Meas. Sci. Technol.* **2022**, *33*, 052001. [CrossRef]
25. Liang, M.; Fang, X. Application of fiber Bragg grating sensing technology for bolt force status monitoring in roadways. *Appl. Sci.* **2018**, *8*, 107. [CrossRef]
26. Pei, H.; Jing, J.; Zhang, S. Experimental study on a new FBG-based and Terfenol-D inclinometer for slope displacement monitoring. *Measurement* **2020**, *151*, 107172. [CrossRef]
27. Montisci, A.; Porcu, M.C. A satellite data mining approach based on self-organized maps for the early warning of ground settlements in urban areas. *Appl. Sci.* **2022**, *12*, 2679. [CrossRef]
28. Komac, M.; Holley, R.; Mahapatra, P.; van der Marel, H.; Bavec, M. Coupling of GPS/GNSS and radar interferometric data for a 3D surface displacement monitoring of landslides. *Landslides* **2015**, *12*, 241–257. [CrossRef]

29. Mulas, M.; Ciccarese, G.; Truffelli, G.; Corsini, A. Integration of digital image correlation of Sentinel-2 data and continuous GNSS for long-term slope movements monitoring in moderately rapid landslides. *Remote Sens.* **2020**, *12*, 2605. [CrossRef]
30. Hamza, V.; Stopar, B.; Sterle, O.; Pavlovčič-Prešeren, P. A cost-effective GNSS solution for continuous monitoring of landslides. *Remote Sens.* **2023**, *15*, 2287. [CrossRef]
31. Lian, X.; Li, Z.; Yuan, H.; Hu, H.; Cai, Y.; Liu, X. Determination of the stability of high-steep slopes by global navigation satellite system (GNSS) real-time monitoring in long wall mining. *Appl. Sci.* **2020**, *10*, 1952. [CrossRef]
32. Sousa, J.J.; Liu, G.; Fan, J.; Perski, Z.; Steger, S.; Bai, S.; Wei, L.; Salvi, S.; Wang, Q.; Tu, J.; et al. Geohazards monitoring and assessment using multi-source earth observation techniques. *Remote Sens.* **2021**, *13*, 4269. [CrossRef]
33. Ding, Q.; Guo, C.; Liu, X.; Gong, X.; Zhou, W.; Ma, G. Multi-source monitoring data helps revealing and quantifying the excavation-induced deterioration of rock mass. *Eng. Geol.* **2023**, *325*, 107281. [CrossRef]
34. Lin, Z.; Jiang, Y.; Xiong, Y.; Xu, C.; Guo, Y.; Wang, C.; Fang, T. Analytical solution for displacement-dependent active earth pressure considering the stiffness of cantilever retaining structure in cohesionless soil. *Comput. Geotech.* **2024**, *170*, 106258. [CrossRef]
35. Cignetti, M.; Godone, D.; Notti, D.; Lanteri, L.; Giordan, D. Impacts on mountain settlements of a large slow rock-slope deformation: A multi-temporal and multi-source investigation. *Landslides* **2024**, *21*, 327–337. [CrossRef]
36. Dai, K.; Li, Z.; Xu, Q.; Tomas, R.; Li, T.; Jiang, L.; Zhang, J.; Yin, T.; Wang, H. Identification and evaluation of the high mountain upper slope potential landslide based on multi-source remote sensing: The Aniangzhai landslide case study. *Landslides* **2023**, *20*, 1405–1417. [CrossRef]
37. Guangdong Provincial Meteorological Bureau, Guangdong Meteorological Yearbook 2023. Available online: https://www.weather.com (accessed on 21 March 2024).
38. Naidu, S.; Sajinkumar, K.S.; Oommen, T.; Anuja, V.J.; Samuel, R.A.; Muraleedharan, C. Early warning system for shallow landslides using rainfall threshold and slope stability analysis. *Geosci. Front.* **2018**, *9*, 1871–1882. [CrossRef]
39. Chen, H.; Zhang, G.; Chang, Z.; Wen, L.; Gao, W. Failure Analysis of a Highway Cut Slope with Anti-Slide Piles. *Geofluids* **2021**, *2021*, 6622214. [CrossRef]

Disclaimer/Publisher's Note: The statements, opinions and data contained in all publications are solely those of the individual author(s) and contributor(s) and not of MDPI and/or the editor(s). MDPI and/or the editor(s) disclaim responsibility for any injury to people or property resulting from any ideas, methods, instructions or products referred to in the content.